Impact ionization processes in a photodriven Mott insulator: influence of phononic dissipation

Paolo Gazzaneo,[1,*] Tommaso Maria Mazzocchi,[1] Jan Lotze,[1] and Enrico Arrigoni[1,†]

[1] *Institute of Theoretical and Computational Physics, Graz University of Technology, 8010 Graz, Austria*

(Dated: August 23, 2022)

We study a model for photovoltaic energy collection consisting of a Mott insulating layer in presence of acoustic phonons, coupled to two wide-band fermion leads at different chemical potentials and driven by a periodic electric field. We treat electron correlations with nonequilibrium dynamical mean-field theory (DMFT) using the so-called auxiliary master equation approach as impurity solver and include dissipation by acoustic phonons via the Migdal approximation. For a small hybridization to the leads, we obtain a peak in the photocurrent as a function of the driving frequency which can be associated with impact ionization processes. For larger hybridizations the shallow peak suggests a suppression of impact ionization with respect to direct photovoltaic excitations. Acoustic phonons slightly enhance the photocurrent for small driving frequencies and suppress it at frequencies around the main peak. This effect occurs at all considered hybridization strengths.

PACS numbers: 71.10.Fd,71.15.-m,71.27+a,71.38.-k,72.20.Jv,73.21.-b,73.21.La,73.50.Pz

I. INTRODUCTION

The idea of designing photovoltaic devices exploiting the Mott gap to convert electromagnetic radiation into energy has become popular in recent years [1–5]. In particular, it has been suggested that in strongly correlated materials, highly excited charge carriers could use their extra energy to excite additional carriers across the Mott gap via impact ionization (II) [1, 4], thus potentially improving their efficiency beyond the Shockley-Queisser limit [6]. Although II is also present in conventional semiconductor devices, the time scales for electron-electron scattering are typically much longer than in correlated materials, so that highly excited electrons will mostly dissipate their energy to phonons.

Experimentally, evidence for fast carrier multiplication processes has been detected via pump-probe experiments in VO_2 [7]. Oxide heterostructures based on $LaVO_3/SrTiO_3$ have been identified as promising candidates, due to the ideal band gap and the strong polar field, able to separate the excited charge carriers [8]. There are however some drawbacks, such as the low mobility of the carriers [5, 9], which still put into question these materials' applicability as efficient solar cells. Thus while a large-scale application of Mott-based solar cells may be difficult to achieve, employing them as photodetectors may be more promising on the long run, due to their high photoresponsivity. From the scientific point of view and for future applications it is thus worthwile to further investigate the properties of Mott-based photovoltaic materials and the mechanisms behind their inner workings, to explore whether alternative unexpected paths can be opened. In fact, a lot of theoretical work has been done to understand the II process (see, e.g. [4, 10–16]).

As a scattering process, II competes with electron-phonon (e-ph) scattering which is the dominant relaxation mechanism in conventional semiconductors. This may not be the case in Mott insulators, at least in certain cases [4]. Therefore, it is essential to understand the influence of e-ph scattering on the photocurrent and II in Mott photovoltaic devices, which is the issue we address in this paper.

For this goal we consider the simplified model shown in Fig. 1, consisting of a Hubbard layer located between two leads. The metallic leads have themselves a wide band, which is effectively narrowed due to the weak coupling to intermediate layers which we take as models for the contacts. Electrons on the Hubbard layer interact locally with acoustic phonons. An external periodic electric field induces a Floquet steady state with a current flowing from the lead with the lower to the higher chemical potential, thus transferring its energy. We address this periodic problem via nonequilibrium Floquet dynamical mean-field theory (F-DMFT).

Our goal is to investigate the occurrence of II in this photovoltaic setup and how it is affected by the presence of phonons. Specifically we study the behavior of the photovoltaic current, the spectral properties as well as the double occupation as a function of the hybridization strength and the properties of the phonons. Our analysis can only provide qualitative results, while quantitative comparisons with experimental systems require a more realistic setup and are beyond the scope of this work.

We find that a small hybridization to the leads is more favorable for II than a larger one. II therefore plays a crucial role in compensating the smaller charge injection, giving the same order of magnitude in the photocurrent as for the larger hybridization. In all cases, the interaction with phonons slightly enhances the photocurrent for small driving frequencies, while suppressing it in vicinity

* paolo.gazzaneo@tugraz.at
† arrigoni@tugraz.at

of the main peak.

The structure of the paper is as follows: in Sec. II we describe the model Hamiltonian. Methods, formalism and observables are presented in Sec. III. We discuss our results in Sec. IV and present our conclusion in Sec. V.

II. MODEL

Our setup introduced in Sec. I and shown in Fig. 1 is described by the Hamiltonian

$$\begin{aligned}\hat{H}(t) = \varepsilon_{\mathrm{c}} \sum_{i\sigma} \hat{n}_{i\sigma} - \sum_{\sigma} \sum_{(i,j)} t_{ij}(t) \hat{c}^{\dagger}_{i\sigma} \hat{c}_{j\sigma} \\ + U \sum_{i} \hat{n}_{i\uparrow} \hat{n}_{i\downarrow} + \hat{H}_{\text{e-ph}} + \hat{H}_{\text{ph}} + \hat{H}_{\text{lead}}.\end{aligned} \tag{1}$$

The operator $\hat{c}^{\dagger}_{i\sigma}$ ($\hat{c}_{i\sigma}$) creates (annihilates) a particle with spin $\sigma = \{\uparrow, \downarrow\}$ on the i-th lattice site and $\hat{n}_{i\sigma} \equiv \hat{c}^{\dagger}_{i\sigma} \hat{c}_{i\sigma}$ is the particle number operator. We denote with (i, j) the sum over nearest-neighbor sites and with $\varepsilon_{\mathrm{c}} \equiv -U/2$ the on-site energy. The driving field consists of a time-periodic, homogeneous and monochromatic electric field with frequency Ω. In the temporal gauge it enters via the Peierls substitution in the time-dependent hopping in Eq. (1) [17]

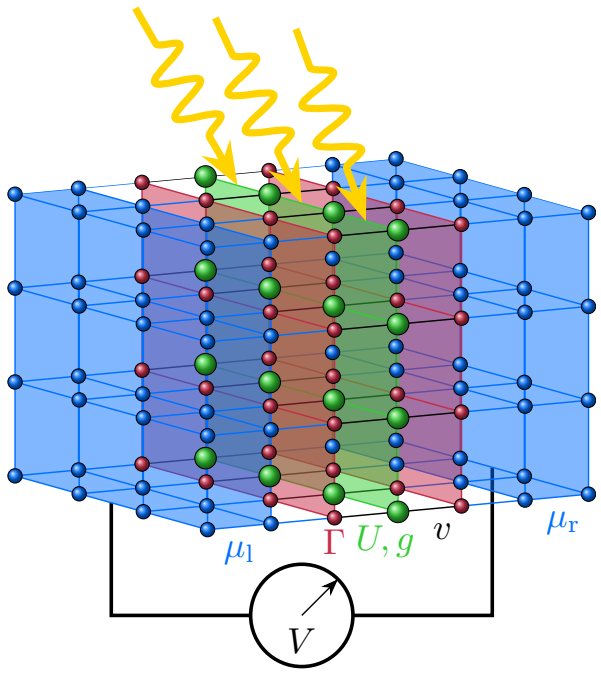

FIG. 1. (Color online) Schematic representation of the setup. A central, correlated layer with local Hubbard interaction U and e-ph coupling g (green) is sandwiched between two non-interacting layers (red) via the hybridization v (black). The latter are in turn coupled to wide-band fermion reservoirs (blue) with different chemical potentials $\mu_{\mathrm{l/r}}$, which introduce a broadening $\Gamma = \Gamma_{\mathrm{l}} = \Gamma_{\mathrm{r}}$.

$$t_{ij}(t) = t_{\mathrm{c}}\ e^{-\mathrm{i}\frac{q}{\hbar}(\boldsymbol{r}_j - \boldsymbol{r}_i)\cdot \boldsymbol{A}(t)}, \tag{2}$$

where t_{c} is the intra-layer hopping, $\boldsymbol{A}$(t) the time-dependent vector potential, $\hbar$ Planck's constant and q the charge of the electrons. Following Refs. [18, 19], we choose for simplicity $\boldsymbol{A}(t) = \boldsymbol{e}_0 A(t)$, which points along the lattice body diagonal $\boldsymbol{e}_0 = (1, 1, \ldots, 1)$. $A(t) = \frac{\hbar}{qa}\mathscr{A}\sin(\Omega t)$ with $\mathscr{A} = -\frac{qE_0 a}{\hbar\Omega}$, E_0 is the electric field amplitude, and a the lattice spacing [18]. In this temporal gauge the electric field is $\boldsymbol{E} = -\partial_t \boldsymbol{A}(t) = \boldsymbol{e}_0 E_0 \cos(\Omega t)$.

The local e-ph coupling is included as in Ref. [20] with an acoustic phonon branch attached to each lattice site via the Hamiltonian

$$\hat{H}_{\text{e-ph}} = g \sum_{i\sigma} \hat{n}_{i\sigma} \hat{x}_i, \tag{3}$$

with g as e-ph coupling and $\hat{x}_i \equiv \frac{1}{\sqrt{2}}\left(\hat{b}^{\dagger}_i + \hat{b}_i\right)$, where $\hat{b}^{\dagger}_i$ ($\hat{b}_i$) creates (annihilates) a phonon of the acoustic branch at site i, with dispersion relation described by $\hat{H}_{\text{ph}}$ [20]. Details on the leads are provided in III B.

For mathematical simplicity [21, 22], we consider the correlated central region as a d-dimensional layer and consider the limit of infinite dimensions $d \to \infty$ by rescaling the hopping as $t_{\mathrm{c}} = t^*/2\sqrt{d}$. Taking $a = 1$, sums over the crystal momentum $\mathbf{k}$ of a generic quantity χ read $\sum_{\mathbf{k}} \chi(\omega, \mathbf{k}) \to \int d\epsilon \int d\bar{\epsilon}\ \rho(\epsilon, \bar{\epsilon}) \chi(\omega; \epsilon, \bar{\epsilon})$ with $\rho(\epsilon, \bar{\epsilon}) = (1/\pi t^{*2}) \exp[-(\epsilon^2 + \bar{\epsilon}^2)/t^{*2}]$ as the joint density of states [18] and with

$$\begin{aligned}\epsilon &= -2t_{\mathrm{c}} \sum_{i=1}^{d} \cos(k_i a), \\ \bar{\epsilon} &= -2t_{\mathrm{c}} \sum_{i=1}^{d} \sin(k_i a).\end{aligned} \tag{4}$$

Within the remainder of this paper we set $\hbar = k_{\mathrm{B}} = a = 1 = -q$, $t^* = 2\sqrt{2}$ [23] and $t_r \equiv \frac{t^*}{2\sqrt{2}} = 1$ as unit of energy.

III. METHOD AND FORMALISM

A. Floquet Green's Function method

To correctly describe the nonequilibrium periodic steady state, we use the Floquet generalization of the nonequilibrium Green's function (NEGF) approach [18]. Every function $G(t, t')$ satisfying the periodicity relation $G(t, t') = G(t + \tau, t' + \tau)$, with $\tau = 2\pi/\Omega$ as the period related to the external driving frequency Ω, may be represented as [18, 24, 25]

$$\underline{G}_{mn}(\omega) = \int \mathrm{d}t_{\text{rel}} \int_{-\tau/2}^{\tau/2} \frac{dt_{\text{av}}}{\tau} \mathrm{e}^{\mathrm{i}[(\omega+m\Omega)t - (\omega+n\Omega)t']} \underline{G}(t, t'), \tag{5}$$

known as the *Keldysh-Floquet* GF. The integration variables $t_{\rm rel} = t - t'$ and $t_{\rm av} = (t + t')/2$ are the relative and average times. Within the rest of this work, we denote a Floquet-represented matrix either as X_{mn} with explicit indices, or use a boldface letter $\mathbf{X}$. The underline indicates the overall *Keldysh* structure

$$\underline{\mathbf{G}} \equiv \begin{pmatrix} \mathbf{G}^{\rm R} & \mathbf{G}^{\rm K} \\ \mathbf{0} & \mathbf{G}^{\rm A} \end{pmatrix}, \tag{6}$$

which contains the *retarded*, *advanced* and *Keldysh* components $\mathbf{G}^{\rm R,A,K}$, where $\mathbf{G}^{\rm A} = (\mathbf{G}^{\rm R})^\dagger$. The *Keldysh* component is defined as $\mathbf{G}^{\rm K} \equiv \mathbf{G}^{>} + \mathbf{G}^{<}$, with $\mathbf{G}^{\lessgtr}$ as *lesser* and *greater* components [26–29].

B. Dyson equation

The lattice Floquet GF of our setup obeys the Dyson equation

$$\underline{\mathbf{G}}^{-1}(\omega_n;\epsilon,\bar\epsilon) = \underline{\mathbf{G}}_0^{-1}(\omega_n;\epsilon,\bar\epsilon) - \underline{\mathbf{\Sigma}}(\omega_n;\epsilon,\bar\epsilon) - \underline{\mathbf{\Sigma}}_{\text{e-ph}}(\omega_n;\epsilon,\bar\epsilon). \tag{7}$$

Therein, the lattice GF of the non-interacting part of the Hamiltonian in Eq. (1) is

$$\underline{G}^{-1}_{0,mn}(\omega_n;\epsilon,\bar\epsilon) = \underline{g}^{-1}_{0,mn}(\omega_n;\epsilon,\bar\epsilon) - \sum_{\rho\in\{\rm l,r\}} v_\rho^2 \underline{g}_{{\rm b},\rho}(\omega_n;\epsilon)\delta_{mn} \tag{8}$$

with $v_{\rm l/r}$ as lead-layer hybridization, $\omega_n \equiv \omega + n\Omega$, $n \in \mathbb{Z}$, and

$$\begin{aligned} \left[g_0^{-1}(\omega_n;\epsilon,\bar\epsilon)\right]^{\rm R}_{mn} &= \left(\omega_n + i0^+ - \varepsilon_{\rm c}\right)\delta_{mn} - \varepsilon_{mn}(\epsilon,\bar\epsilon), \\ \left[g_0^{-1}(\omega_n;\epsilon,\bar\epsilon)\right]^{\rm K}_{mn} &= 0 \end{aligned} \tag{9}$$

as the noninteracting Green's function of the isolated layer, whose inverse Keldysh component is negligible in the steady state. The Floquet dispersion relation ε_{mn} for the periodic field in a hyper-cubic lattice is [18]

$$\varepsilon_{mn}(\epsilon,\bar\epsilon) = \begin{cases} \epsilon J_{m-n}(\mathscr{A}) & m-n : \text{even}, \\ \mathrm{i}\,\bar\epsilon J_{m-n}(\mathscr{A}) & m-n : \text{odd}, \end{cases} \tag{10}$$

where J_n denotes the n-th order Bessel function of the first kind, with the argument $\mathscr{A}$ defined in Sec. II. The GF $\underline{g}_{\rm b,l/r}$ on the d-dimensional boundary of the decoupled leads, consisting of a single layer coupled to a semi-infinite reservoir in the wide-band limit with broadening $\Gamma_{\rm l/r}$ (cf. Fig. 1) is given by

$$g^{\rm R}_{\rm b,l/r}(\omega;\epsilon) = \frac{1}{\omega - \varepsilon_{\rm l/r}(\epsilon) + \mathrm{i}\,\Gamma_{\rm l/r}}, \tag{11}$$

$$g^{\rm K}_{\rm b,l/r}(\omega;\epsilon) = 2\,\mathrm{i}\,\mathrm{Im}[g^{\rm R}_{\rm b,l/r}(\omega;\epsilon)][1 - 2f(\omega,\mu_{\rm l/r},\beta)], \tag{12}$$

where $\varepsilon_{\rm l/r}(\epsilon) = \varepsilon_{\rm l/r} + \frac{t_{\rm l/r}}{t^*}\epsilon$ is the dispersion, $f(\omega,\mu_{\rm l/r},\beta) = 1/[\mathrm{e}^{\beta(\omega-\mu_{\rm l/r})}+1]$ the Fermi-Dirac distribution function at inverse temperature $\beta \equiv 1/T$, $\varepsilon_{\rm l/r}$ the on-site energy and $t_{\rm l/r}$ the hopping within the d-dimensional layer of the lead.

The electron self-energy (SE) $\underline{\mathbf{\Sigma}}$ is obtained from F-DMFT and therefore independent of the crystal momentum, i.e. $\underline{\mathbf{\Sigma}}(\omega;\epsilon,\bar\epsilon) \simeq \underline{\mathbf{\Sigma}}(\omega)$. Further details are given in Sec. III C.

The e-ph SE is also included locally as $\underline{\mathbf{\Sigma}}_{\text{e-ph}}(\omega;\epsilon,\bar\epsilon) \simeq \underline{\mathbf{\Sigma}}_{\text{e-ph}}(\omega)$. In terms of the Keldysh contour time arguments z and z', it has the form

$$\Sigma_{\text{e-ph}}(z,z') = \mathrm{i}\,g^2 G(z,z') D_{\rm ph}(z,z'). \tag{13}$$

The Keldysh components of the non-interacting phonon GF $\underline{D}_{\rm ph}(t,t')$ are given by [22]

$$\begin{aligned} D^{\rm R}_{\rm ph}(t,t') &= -\,\mathrm{i}\,\theta(t-t')\int \mathrm{d}\omega\ \mathrm{e}^{-\,\mathrm{i}\,\omega(t-t')} A_{\rm ph}(\omega), \\ D^{>}_{\rm ph}(t,t') &= -\,\mathrm{i}\int \mathrm{d}\omega\ \mathrm{e}^{-\,\mathrm{i}\,\omega(t-t')} A_{\rm ph}(\omega)\,[1+b(\omega)], \\ D^{<}_{\rm ph}(t,t') &= -\,\mathrm{i}\int \mathrm{d}\omega\ \mathrm{e}^{-\,\mathrm{i}\,\omega(t-t')} A_{\rm ph}(\omega)\ b(\omega), \end{aligned} \tag{14}$$

where $b(\omega) = 1/(\mathrm{e}^{\beta\omega} - 1)$ is the Bose-Einstein distribution function at inverse temperature β. We focus on acoustic phonons, with spectral function $A_{\rm ph}(\omega) = (\omega/\omega_{\rm ph}^2)\mathrm{e}^{-|\omega|/\omega_{\rm ph}}$, $\omega_{\rm ph}$ being a soft cutoff frequency [30]. The retarded and Keldysh components of the e-ph SE are easily extracted from Eq. (13) and can be found in Ref. [20].

C. Floquet DMFT

We compute the electron SE in the Dyson Equation (7) using DMFT [21, 31, 32], and in particular its nonequilibrium Floquet extension F-DMFT [18, 24, 25]. In DMFT the crystal momentum dependence of the electron SE is neglected, i.e. $\underline{\mathbf{\Sigma}}(\omega,\epsilon,\bar\epsilon) \to \underline{\mathbf{\Sigma}}(\omega)$. This allows us to map the original lattice problem onto a single-site impurity model with a bath hybridization function $\underline{\mathbf{\Delta}}(\omega)$ encoding the effect of all other lattice sites.

We briefly describe now the self-consistent F-DMFT scheme used. (i) We start from an initial guess for the electron SE $\underline{\mathbf{\Sigma}}(\omega)$ and set $\underline{\mathbf{\Sigma}}_{\text{e-ph}}(\omega) = 0$. (ii) Then we compute the local electron GF as

$$\begin{aligned} \underline{\boldsymbol{G}}_{\rm loc}(\omega) = \int \mathrm{d}\epsilon \int \mathrm{d}\bar\epsilon\ \rho(\epsilon,\bar\epsilon)\times \\ \times \left[\underline{\boldsymbol{G}}_0^{-1}(\omega,\epsilon,\bar\epsilon) - \underline{\mathbf{\Sigma}}(\omega) - \underline{\mathbf{\Sigma}}_{\text{e-ph}}(\omega)\right]^{-1}. \end{aligned} \tag{15}$$

(iii) Using Eq. (13), we obtain the phonon contribution to the SE $\underline{\mathbf{\Sigma}}_{\text{e-ph}}(\omega)$. (iv) The problem is mapped onto a single impurity plus bath, whose hybridization function is given by

$$\underline{\mathbf{\Delta}}(\omega) = \underline{\boldsymbol{g}}^{-1}_{0,\rm site}(\omega) - \underline{\boldsymbol{G}}^{-1}_{\rm loc}(\omega) - \underline{\mathbf{\Sigma}}(\omega), \tag{16}$$

where $\underline{\boldsymbol{g}}^{-1}_{0,\mathrm{site}}(\omega)$ is defined as in Eq. (9) with $\varepsilon_{mn}(\epsilon,\bar{\epsilon})=0$. (v) The nonequilibrium many-body impurity problem is solved according to the procedure in Sec. III C 2, leading to the new $\underline{\boldsymbol{\Sigma}}(\omega)$. (vi) We insert the electron and e-ph SEs into step (ii) and iterate the steps (ii)-(vi) until convergence.

1. *Floquet-diagonal self-energy approximation*

From Eq. (16), we obtain the bath hybridization function $\underline{\boldsymbol{\Delta}}(\omega)$ whose periodic time-dependence is encoded in its Floquet structure. Being interested in photovoltaic effects, we follow Ref. [14] and use the Floquet-diagonal self-energy approximation (FDSA) for which Floquet off-diagonal terms in the electron SE $\underline{\boldsymbol{\Sigma}}(\omega)$ are neglected. In addition, we employ FDSA also for the phonon SE $\underline{\boldsymbol{\Sigma}}_{\text{e-ph}}(\omega)$ [33]. Consequently, we only consider the $(0,0)$-Floquet matrix element of Eq. (16) in the impurity problem, which therefore becomes stationary. It is sufficient to restrict oneself to the $(0,0)$ component, since the other diagonal components can be reconstructed by using the property $\underline{\Sigma}_{mm}(\omega)=\underline{\Sigma}_{00}(\omega+m\Omega)$.

2. *Auxiliary master equation approach*

In the following, we briefly summarize the impurity solver used in step (v) of the DMFT self-consistent loop described in Sec. III C. In order to solve the many-body problem, we use the auxiliary master equation approach (AMEA) [34–37]. Therein, we map the impurity problem onto an auxiliary open quantum system (AOQS) consisting of a finite number of bath sites N_{B} attached to Markovian reservoirs described by the Lindblad equation. The hybridization function $\underline{\Delta}_{\mathrm{aux}}(\omega)$ of this AOQS is obtained by fitting the original DMFT one. The key point is that the many-body problem of this AOQS can be solved exactly using standard many-body-diagonalization methods, as long as N_{B} is small. The accuracy of this solution is set by the difference between $\underline{\Delta}_{\mathrm{aux}}$ and $\underline{\Delta}$, which becomes exponentially small with increasing N_{B}.

D. Physical quantities

To study direct excitation and II effects in this system, we consider the following time-averaged physical quantities.

The photocurrent flowing from the left fermion lead to the right one, passing through the correlated layer is given by

$$j_{\mathrm{l}\to\mathrm{r}} = v^2 \int_{-\Omega/2}^{\Omega/2} \frac{\mathrm{d}\omega}{2\pi} \int \mathrm{d}\epsilon \int \mathrm{d}\bar{\epsilon}\rho(\epsilon,\bar{\epsilon})\,\mathrm{Re}\,\mathrm{Tr}(\boldsymbol{J}) \tag{17}$$

$$= v^2 \int_{-\infty}^{+\infty} \frac{\mathrm{d}\omega}{2\pi} \int \mathrm{d}\epsilon \int \mathrm{d}\bar{\epsilon}\rho(\epsilon,\bar{\epsilon})\,\mathrm{Re}(J_{00}), \tag{18}$$

where

$$\boldsymbol{J} = \left[\boldsymbol{G}^{\mathrm{R}}(\boldsymbol{g}^{\mathrm{K}}_{\mathrm{b,l}}-\boldsymbol{g}^{\mathrm{K}}_{\mathrm{b,r}}) + \boldsymbol{G}^{\mathrm{K}}(\boldsymbol{g}^{\mathrm{A}}_{\mathrm{b,l}}-\boldsymbol{g}^{\mathrm{A}}_{\mathrm{b,r}})\right] \tag{19}$$

is taken from Ref. [14]. Of the two equivalent expressions, Eq. (18) is used in practice.

The local electronic spectral function (DOS) reads

$$A(\omega) = -\frac{1}{\pi}\,\mathrm{Im}[G^{\mathrm{R}}_{\mathrm{loc},00}(\omega)], \tag{20}$$

where $G^{\mathrm{R}}_{\mathrm{loc},00}$ is the time-averaged retarded component of the GF given in Eq. (15). Combining it with the time-averaged Keldysh component gives the occupation function

$$N(\omega) = \frac{1}{4\pi}[\mathrm{Im}(G^{\mathrm{K}}_{\mathrm{loc},00}) - 2\,\mathrm{Im}(G^{\mathrm{R}}_{\mathrm{loc},00})]. \tag{21}$$

IV. RESULTS

In order to study II in a Mott insulating layer, we set the bands to achieve the energy scheme shown in Fig. 2(a).

We follow Ref. [14] and choose $U=12$ and $E_0=2$. The fermion leads and acoustic phonons have temperature $T=0.02$. We consider a particle-hole symmetric system with $\Gamma_{\mathrm{l}}=\Gamma_{\mathrm{r}}=0.37$, $t_{\mathrm{l}}=t_{\mathrm{r}}=1.7$, $\varepsilon_{\mathrm{l/r}}=\mp 6$ and $v_{\mathrm{l}}=v_{\mathrm{r}}=v$. The parameters $t_{\mathrm{l/r}}$, $\varepsilon_{\mathrm{l/r}}$, and $\Gamma_{\mathrm{l/r}}$ are chosen such that the leads' DOS approximately coincides with the Hubbard bands, i.e. they exhibit a 'bandwidth' [38] $W_{\mathrm{b}}\approx 8$ and are centered at the same position. The chemical potentials are set to $\mu_{\mathrm{l/r}}=\mp 1$, so that a current from left to right is produced by energy taken from the driving.

Due to the hybridization with the leads, the local DOS of the Hubbard layer only features a pseudogap $\Delta_{\mathrm{pg}}\approx 4$. All simulations are carried out with the dimensionless factor $\alpha\equiv t_r E_0/\Omega^2<0.5$ for which the FDSA is justified [39] and first-order photon absorption processes are dominant. Whenever the electron-phonon interaction is switched on, we take $g=0.8$ and unless stated otherwise $\omega_{\mathrm{ph}}=0.1$.

After some preliminary considerations in Sec. IV A, we will discuss the occurrence of II at different v first without (Sec. IV B) and then with coupling to acoustic phonons (Sec. IV C).

A. Energy considerations and physical processes

To infer the conditions necessary for II, we consider the scheme in Fig. 2. Thereby, we partially follow Ref. [14] for the electron-only (EO) case and extend the analysis to the case with e-ph interaction. Here, we also consider a more realistic structure of the leads. As in Ref. [14] we bypass transient behavior and consider directly the nonequilibrium Floquet steady state. In our analysis,

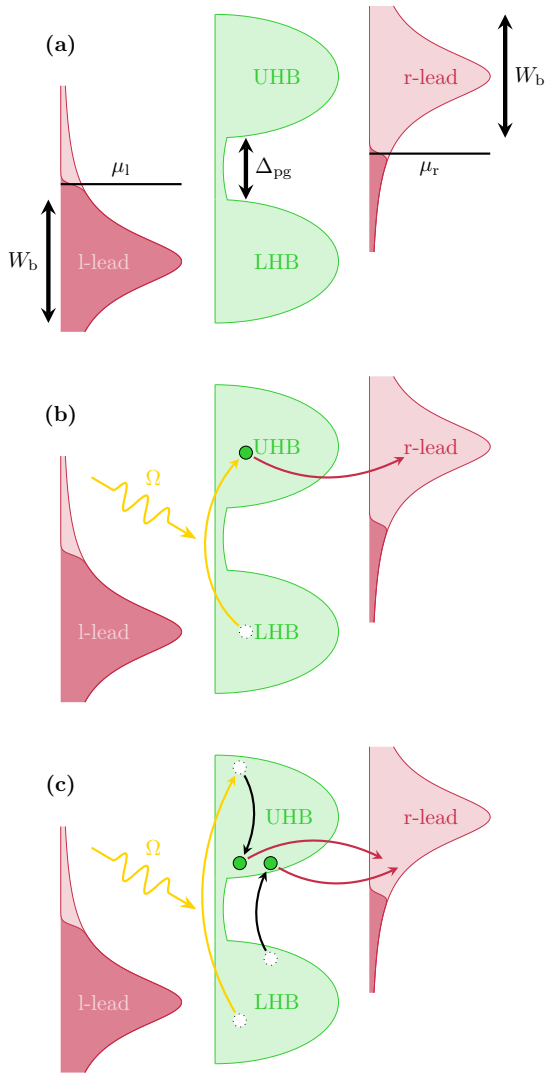

FIG. 2. (Color online) Schematic representation of the processes occuring in the model considered. Red bands on the left and right describe the leads' DOS, where the dark color highlights occupied states and the light color empty states. Green bands are the LHB and UHB of the central layer. The vertical axis represents the energy. Panel (a) sketches the quantities introduced at the beginning of Sec. IV. Panel (b) illustrates a direct excitation process, in which an electron is excited by a photon with energy Ω (yellow arrow) to the UHB and escapes into the right lead (red arrow). Panel (c) displays an II process, where the photoexcited electron in the UHB excites a second electron from LHB to UHB (black arrows) and both escape into the right lead. In the nonequilibrium steady state considered here, only processes recovering the initial configuration are allowed.

we neglect higher-order processes such as multiparticle scattering II processes.

In order to observe II, the bandwidth of the UHB has to be at least twice the pseudogap size Δ_{pg}. Only in this case, the photoexcited electron can acquire enough energy to excite a second one across the pseudogap.

1. *EO system*

- For $\Omega < \Delta_{pg}$, we do not expect any current if the DOS of the correlated layer has a true gap [40]. If Δ_{pg} is a partial gap, we expect a suppression of the current.
- For $\Delta_{pg} < \Omega < \Delta_{pg}+2W_b$ as shown in Fig. 2(b), an electron coming from the left lead into the LHB is photoexcited to the UHB and can escape directly into the right lead without additional scattering. We will refer to such processes as direct excitations (DEs).
- For $2\Delta_{pg} < \Omega < \Delta_{pg} + 2W_b$ as shown in Fig. 2(c), a photoexcited electron in the UHB can excite via II a second electron from LHB to UHB, before both escape into the right lead.
- For $\Omega > \Delta_{pg} + 2W_b$, there are no final states available for a photoexcited electron and we do not expect the transition to occur.

Notice that in the energy window $\Delta_{pg} < \Omega < 2\Delta_{pg}$ the only scattering processes taking place are DEs, while for $2\Delta_{pg} < \Omega < \Delta_{pg} + 2W_b$, both DE and II can occur. We want to stress however, that the boundaries of these energy ranges are not strict and that it is difficult to disentangle the effects of these physical processes.

2. *Inclusion of e-ph interactions*

Upon inclusion of e-ph scattering, the outlined scheme remains valid except for a modification of the pseudogap Δ_{pg}. As shown in Sec. IV C, the phonons broaden the DOS of the correlated layer and slightly fill the pseudogap. Therefore the pseudogap is reduced by a small amount indicating the dissipation by phonons.

B. EO system

We start with the EO case without e-ph interaction and investigate the dependence of the physical quantities on the lead-layer hybridization.

In Fig. 3(a), the photocurrent j increases as a function of the driving frequency Ω within the range $4 \lesssim \Omega \lesssim 8$ independent of the value of v. According to the discussion in Sec. IV A 1 (cf. Fig. 2), this Ω-range is expected to allow only for DEs. The current in this range increases with increasing v. Similarly, the double occupation shown in Fig. 3(b) increases as a function of the driving frequency [41].

For $\Omega \gtrsim 8$, the current increases further until it reaches its peak at $\Omega \approx 11$. In this range both DE and II can occur. The height of the peak is approximately the same for both v, despite the lead-layer hybridizations differing by a factor of two. The double occupation in this range

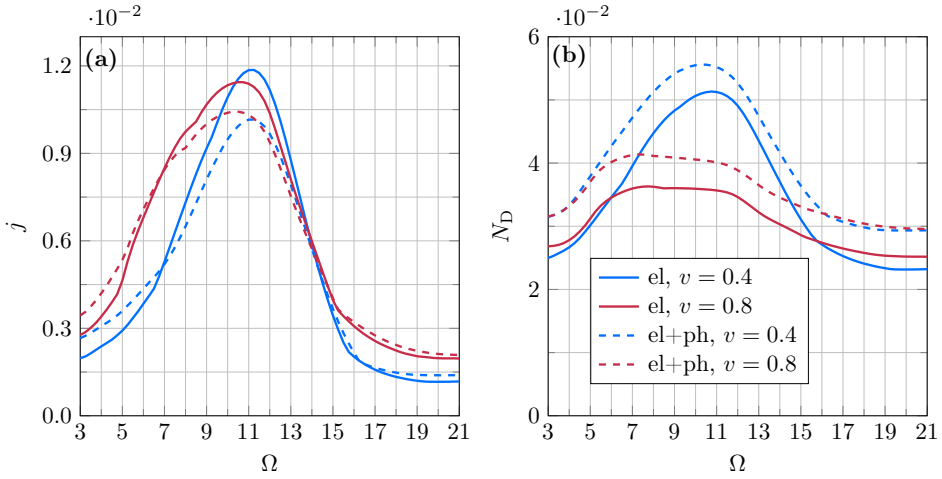

FIG. 3. (Color online) (a) Time-averaged steady-state current j and (b) double occupancy N_D plotted as a function of the driving frequency Ω. Results are shown for different values of the lead-layer hybridization v as well as without and with e-ph interaction. Default parameters are specified at the beginning of Sec. IV.

shows a similar behavior as the current for $v = 0.4$ with a peak around $\Omega \approx 11$, while it exhibits a plateau for $v = 0.8$. For $v = 0.4$ the current curve is characterized by a substantial change in slope around $\Omega \approx 8$, which is absent for $v = 0.8$. This, together with the comparable magnitude of the maxima at $\Omega \approx 11$ and the behavior of the double occupation strongly suggest that for $v = 0.4$ a substantial number of II processes take place, while these are absent or negligible for $v = 0.8$. Here, the plateau in N_D for $v = 0.8$ suggests that photoexcited electrons arriving in the UHB quickly escape to the right fermionic lead and do not have time to induce II processes.

The spectral and occupation function shown in Fig. 4 corroborate this hypothesis. For $\Omega = 5$ in the DE range, the occupation function in the UHB is almost the same for both v, while for $\Omega = 11$ where the peak in the current occurs, the occupation of the UHB for $v = 0.4$ is substantially larger, in line with the behavior of N_D.

Finally, increasing Ω further, decreases the current and

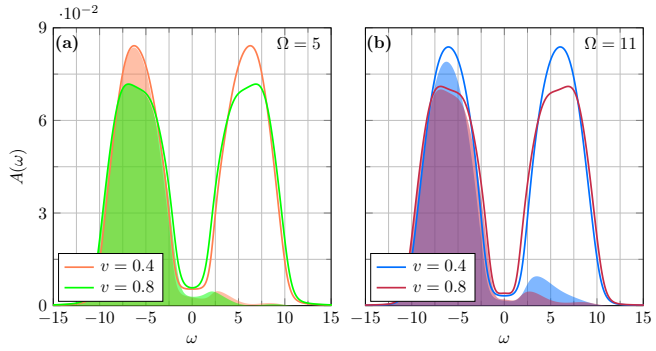

FIG. 4. (Color online) Spectral function $A(\omega)$ (solid line) and occupation function $N(\omega)$ (shaded area) at (a) $\Omega = 5$ and (b) $\Omega = 11$ for $v = 0.4$ and 0.8 for the EO system. Default parameters are specified at the beginning of Sec. IV.

double occupation [42].

C. Inclusion of e-ph interactions

We now discuss the effect of coupling to acoustic phonons on the results discussed above.

The current j in presence of phonons shown in Fig. 3(a) is slighty larger than the EO one for $\Omega \lesssim 7$. This effect is reduced with increasing Ω until a crossing occurs at $\Omega \approx 7$ where the EO current overtakes. Between $7 \lesssim \Omega \lesssim 14$, the current in the presence of phonons exhibits the same qualitative behavior as the EO one, reaching its maximum at $\Omega \approx 11$. However the current magnitude is suppressed, especially around the peak. For $\Omega \gtrsim 14$ the current with phonons goes down as for the EO case.

The double occupation N_D shown in Fig. 3(b) is larger than and follows the behavior of its EO counterpart within the entire Ω-range considered. The spectral and occupation function shown in Fig. 5 display a redistribution of spectral weight from the peaks towards the edges of the bands, thus reducing the pseudogap. Consequently, the occupation of positive energy states is slightly shifted to the bottom of the UHB compared to the EO case, as the occupation function shows. The spectral function in presence of phonons is broadened and tends to fill the pseudogap Δ_{pg} as anticipated in Sec. IV A 2. This reduction of the pseudogap explains why the current in Fig. 3(a) is slightly larger in presence of phonons for $\Omega \lesssim 7$. With a smaller pseudogap and more states at its edges, more electrons can be directly excited with a given driving frequency thereby increasing the photocurrent. On the other hand, the suppression of the current by e-ph interaction in the range $7 \lesssim \Omega \lesssim 14$ is due to the reduction of spectral weight at frequencies $|\omega| \gtrsim 3.5$, cf. Fig. 5.

The increase of the double occupation N_D seen in

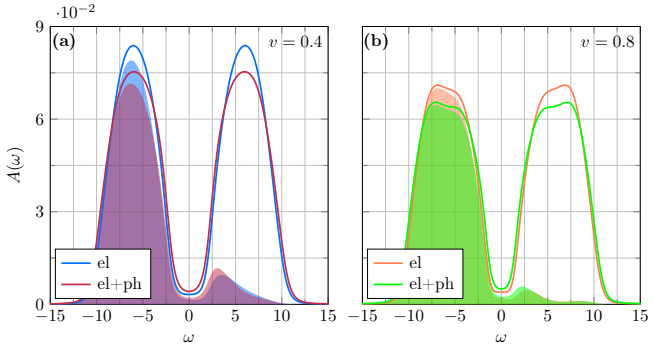

FIG. 5. (Color online) Spectral function $A(\omega)$ (solid line) and occupation function $N(\omega)$ (shaded area) at $\Omega = 11$ without and with e-ph interaction, for (a) $v = 0.4$ and (b) $v = 0.8$. Default parameters are specified at the beginning of Sec. IV.

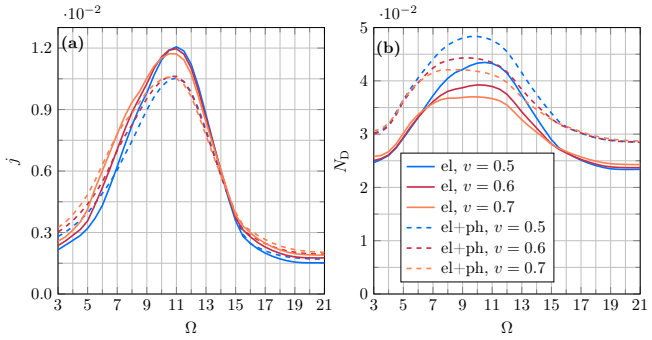

FIG. 7. (Color online) (a) Time-averaged steady-state current j and (b) double occupancy N_D as a function of Ω, for $v = 0.5, 0.6, 0.7$, without and with e-ph interaction. Default parameters are specified at the beginning of Sec. IV.

Fig. 3(b) for the case with phonons can already be inferred from the occupation function $N(\omega)$ at positive frequencies depicted in Fig. 5.

Summarizing, phonons enhance the current for almost all driving frequencies $\Omega \lesssim 7$ for which only DEs take place. They suppress the current in the range $7 \lesssim \Omega \lesssim 14$, where II is the dominant electronic scattering process for $v = 0.4$ and DE for $v = 0.8$.

This is confirmed by Fig. 6, which shows that the impact of acoustic phonons on current and double occupation is slightly boosted when decreasing the soft cutoff frequency ω_{ph} [43].

The results above suggest that the influence of acoustic phonons on the electronic scattering processes is similar for all values of v, independent of how it affects DE or II. In other words, the effects of phonons is independent of the rate at which carriers are injected into and removed from the layer. Fig. 7 confirms this behavior for intermediate lead-layer hybridizations $v = 0.5, 0.6, 0.7$, for which DE and II at $\Omega \gtrsim 8$ are even stronger mixed and harder to separate. Also the location of the crossing in the current between the EO and e-ph case is essentially independent of v, as can be seen in Fig. 7(a). The increase

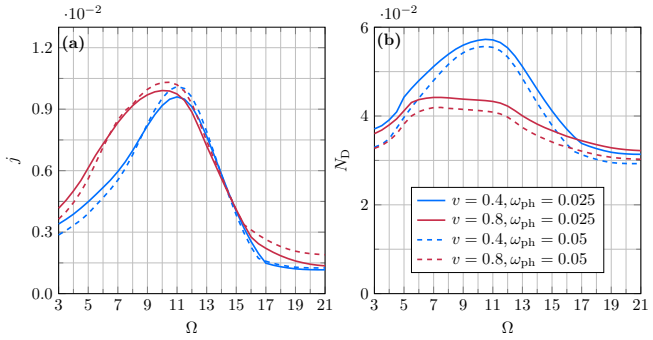

FIG. 6. (Color online) (a) Time-averaged steady-state current j and (b) double occupancy N_D as a function of Ω, for $v = 0.4, 0.8$, at phonon cutoff frequencies $\omega_{\text{ph}} = 0.025, 0.05$. Default parameters are specified at the beginning of Sec. IV.

of double occupation for the case with e-ph interaction (cf. Fig. 3(b)-Fig. 7(b)) coincides with the current suppression and is probably due to a stronger localization of photoexcited electrons in the UHB.

V. CONCLUSION

We investigated the influence of fermion leads and phonon dissipation on electron transport and spectral properties of a Mott insulating layer driven to the nonequilibrium steady state by an external periodic field. In order to realize a Mott-based photovoltaic setup between metallic leads, we considered a correlated layer coupled to acoustic phonons, located between wide-band fermion leads. We demonstrated the importance of coupling to fermion leads for the electron scattering process occurring at different driving frequencies and observed how the dissipation by acoustic phonons influences the photocurrent and the double occupation. We found strong evidence that the dominant electron scattering mechanism responsible for the photocurrent peak at small hybridizations to the fermion leads is II, while DEs dominate at higher hybridizations. Dissipation via acoustic phonons slightly boosts the photocurrent for small driving frequencies and suppresses it at higher ones in the vicinity of the main peak. The effect of phonons is not affected by changes in the lead-layer hybridization.

These results suggest that in systems where correlated layers are connected to metallic leads via weakly coupled single layers or molecules, II could contribute significantly to the photocurrent. From the experimental point of view, such setup is employed, for example, to bridge semiconductor quantum dots to reservoirs through small molecules [44, 45] to extract hot photoexcited carriers [46, 47]. Based on our results, moderate e-ph coupling does not suppress the photocurrent significantly and therefore in real materials, II could contribute to overcome the Schockley-Queisser limit [6].

Experimentally, the electric field amplitude considered in this paper [48] is several orders of magnitude larger

than that of the sunlight, however it is possible to achieve such amplitudes via THz pulses [19]. Moreover, in order to address the occurrence of II in realistic photovoltaic setups, one should extend such simplified model to multiorbital systems [13] in a multilayer setup, to model oxide heterostructures [8, 13] where the correlated region consists of multiple layers and photoexcited carriers are separated via an electric field gradient. Another step forward would be to take into account the effect of impurity scattering and the feedback of the electrons onto the phonon dynamics with a self-consistent treatment.

ACKNOWLEDGEMENTS

We thank A. Picano for fruitful discussions. This work was supported by the Austrian Science Fund (FWF) within Project P 33165-N, as well as NaWi Graz. The computational results presented have been obtained using the Vienna Scientific Cluster (VSC) and the D-Cluster Graz.

[1] E. Manousakis, Phys. Rev. B **82**, 125109 (2010).
[2] H. Liang, L. Cheng, X. Zhai, N. Pan, H. Guo, J. Zhao, H. Zhang, L. Li, X. Zhang, X. Wang, C. Zeng, Z. Zhang, and J. G. Hou, Sci. Rep. **3**, 1 (2013).
[3] H.-Z. Guo, L. Gu, Z.-Z. Yang, S.-F. Wang, G.-S. Fu, L. Wang, K.-J. Jin, H.-B. Lu, C. Wang, C. Ge, M. He, and G.-Z. Yang, Europhys. Lett. **103**, 47006 (2013).
[4] J. E. Coulter, E. Manousakis, and A. Gali, Phys. Rev. B **90**, 165142 (2014).
[5] L. Wang, Y. Li, A. Bera, C. Ma, F. Jin, K. Yuan, W. Yin, A. David, W. Chen, W. Wu, W. Prellier, S. Wei, and T. Wu, Phys. Rev. Applied **3**, 064015 (2015).
[6] W. Shockley and H. J. Queisser, Journal of Applied Physics **32**, 510 (1961).
[7] J. Holleman, M. M. Bishop, C. Garcia, J. S. R. Vellore Winfred, S. Lee, H. N. Lee, C. Beekman, E. Manousakis, and S. A. McGill, Phys. Rev. B **94**, 155129 (2016).
[8] E. Assmann, P. Blaha, R. Laskowski, K. Held, S. Okamoto, and G. Sangiovanni, Phys. Rev. Lett. **110**, 078701 (2013).
[9] M. Jellite, J.-L. Rehspringer, M. Fazio, D. Muller, G. Schmerber, G. Ferblantier, S. Colis, A. Dinia, M. Sugiyama, A. Slaoui, D. Cavalcoli, and T. Fix, Solar Energy **162**, 1 (2018).
[10] M. Eckstein and P. Werner, Phys. Rev. B **84**, 035122 (2011).
[11] M. Eckstein and P. Werner, Phys. Rev. B **88**, 075135 (2013).
[12] P. Werner, K. Held, and M. Eckstein, Phys. Rev. B **90**, 235102 (2014).
[13] F. Petocchi, S. Beck, C. Ederer, and P. Werner, Phys. Rev. B **100**, 075147 (2019).
[14] M. E. Sorantin, A. Dorda, K. Held, and E. Arrigoni, Phys. Rev. B **97**, 115113 (2018).
[15] A. Kauch, P. Worm, P. Prauhart, M. Innerberger, C. Watzenböck, and K. Held, Phys. Rev. B **102**, 245125 (2020).
[16] F. Maislinger and H. G. Evertz, Phys. Rev. B **105**, 045114 (2022).
[17] R. Peierls, Zeitschrift für Physik A Hadrons and Nuclei **80**, 763 (1933).
[18] N. Tsuji, T. Oka, and H. Aoki, Phys. Rev. B **78**, 235124 (2008).
[19] Y. Murakami and P. Werner, Phys. Rev. B **98**, 075102 (2018).
[20] T. M. Mazzocchi, P. Gazzaneo, J. Lotze, and E. Arrigoni, arXiv:2207.01921 (unpublished).
[21] A. Georges and G. Kotliar, Phys. Rev. B **45**, 6479 (1992).
[22] H. Aoki, N. Tsuji, M. Eckstein, M. Kollar, T. Oka, and P. Werner, Rev. Mod. Phys. **86**, 779 (2014).
[23] With such choice for t^* we reproduce the DOS of a 2D layer with $t_c = 1$ in order to compare with Ref. [14].
[24] P. Schmidt and H. Monien, cond-mat/0202046 (unpublished).
[25] A. V. Joura, J. K. Freericks, and T. Pruschke, Phys. Rev. Lett. **101**, 196401 (2008).
[26] J. Schwinger, J. Math. Phys. **2**, 407 (1961).
[27] L. V. Keldysh, Sov. Phys. JETP **20**, 1018 (1965).
[28] J. Rammer and H. Smith, Rev. Mod. Phys. **58**, 323 (1986).
[29] H. Haug and A.-P. Jauho, *Quantum Kinetics in Transport and Optics of Semiconductors* (Springer, Heidelberg, 1998).
[30] A. Picano, J. Li, and M. Eckstein, Phys. Rev. B **104**, 085108 (2021).
[31] W. Metzner and D. Vollhardt, Phys. Rev. Lett. **62**, 324 (1989).
[32] A. Georges, G. Kotliar, W. Krauth, and M. J. Rozenberg, Rev. Mod. Phys. **68**, 13 (1996).
[33] In the parameters range in which FDSA is justified for the electron SE $\underline{\mathbf{\Sigma}}(\omega)$ (Sec. IV), the diagonal terms of the phonon SE $\underline{\Sigma}_{mm,\text{e-ph}}(\omega)$ are orders of magnitude bigger than the off-diagonal ones.
[34] E. Arrigoni, M. Knap, and W. von der Linden, Phys. Rev. Lett. **110**, 086403 (2013).
[35] A. Dorda, M. Nuss, W. von der Linden, and E. Arrigoni, Phys. Rev. B **89**, 165105 (2014).
[36] A. Dorda, M. Ganahl, H. G. Evertz, W. von der Linden, and E. Arrigoni, Phys. Rev. B **92**, 125145 (2015).
[37] A. Dorda, M. Sorantin, W. von der Linden, and E. Arrigoni, New J. Phys. **19**, 063005 (2017).
[38] Notice that the support of its spectrum is formally infinite. W_b is the value at which the spectrum gets suppressed.
[39] In Ref. [14] the factor is defined as $\alpha = t_c E_0/\Omega^2$ and $t_c = 1$. Setting $t_r = 1$, we define for consistency α as in the main text.
[40] To overcome a true gap with $\Omega < \Delta_{pg}$ multiple-photon absorption processes should take place, but as written in the main text, such effects are negligible in the studied parameters range.

[41] Notice that the increase of N_{D} in Fig. 3(b) as compared to Ref. [14] is not as steep and large in magnitude. This is due to our setup, where every photoexcited carrier can escape to the right lead.
[42] The current j does not approach zero as expected for $\Omega > 20$ because of the background current as discussed in Ref. [14].
[43] Reducing ω_{ph} has two effects. First, the spectral function $A_{\mathrm{ph}}(\omega)$ exhibits more weight at low frequencies $\omega \approx \omega_{\mathrm{ph}}$. Second, it restricts the maximal value of the reciprocal lattice vector $\boldsymbol{q}_{\mathrm{max}}$ via $\omega_{\mathrm{ph}} = \omega(\boldsymbol{q}_{\mathrm{max}})$ [20], meaning that short-wavelength phonons are neglected.
[44] H. Wang, E. R. McNellis, S. Kinge, M. Bonn, and E. Cánovas, Nano Letters **13**, 5311 (2013), pMID: 24093529.
[45] H. I. Wang, M. Bonn, and E. Cánovas, The Journal of Physical Chemistry Letters **8**, 2654 (2017).
[46] W. Tisdale, K. Williams, B. Timp, D. Norris, E. Aydil, and X. Zhu, Science **328**, 1543 (2010).
[47] E. Cánovas, H. Wang, M. Karakus, and M. Bonn, Chemical Physics **471**, 54 (2016), carrier Dynamics in Quantum Confined Semiconductor Nanocrystals.
[48] We do not consider smaller electric field amplitudes E_0 since DMFT only converges slowly for such a choice of parameters. Moreover, the observables' magnitude becomes comparable to our numerical precision.